metals

MDPI

Article

Effect of the Filler Metal and Shielding Gas on the Fatigue Life in HSLA Steels Welded Using the GMAW Process

Francisco Briones [1,*], Henrique Soares Zanin [2], Roberto Iquilio Abarzúa [1] and William Haupt [2]

[1] Escuela de Ingeniería Mecánica, Pontificia Universidad Católica de Valparaíso, Los Carrera, Quilpué 01567, Chile; roberto.iquilio@pucv.cl
[2] Mechanical Engineering, University of Passo Fundo, Passo Fundo, Br 285 km 292, Passo Fundo 99052-900, Brazil; 168426@upf.br (H.S.Z.); williamhaupt@upf.br (W.H.)
* Correspondence: francisco.briones@pucv.cl

Abstract: The composition of the filler electrodes, as well as the shielding gases, has a strong impact on the static and dynamic properties of welded joints in HSLA steels. The content of Cr, Ni, and Mo, along with the shielding gases, helps maintain the hardness values in the HAZ of HSLA steels welded using the GMAW process, resulting in a positive impact on the fatigue life of the joints. Maintaining fatigue properties in the regions of the heat-affected zone is crucial. The increase in the size of the HAZ, coupled with microstructural changes, leads to a reduction in the hardness values in this region, contributing to a decrease in the fatigue life of welded joints. In this study, the effects of using different filler electrodes and shielding gases on the fatigue properties of welded joints in LNE 600 steel with a thickness of 4.75 mm, welded using the GMAW process, were evaluated. It was possible to observe a reduction in the hardness values in the HAZ region and a similar static resistance behavior for all evaluated conditions, except for the ER70S-6 electrode with 5% O_2 gas, where the fatigue life showed better results with the application of the ER120S-G electrode.

Keywords: HSLA steels; agricultural machinery; fatigue welds

check for updates

Citation: Briones, F.; Zanin, H.S.; Iquilio Abarzúa, R.; Haupt, W. Effect of the Filler Metal and Shielding Gas on the Fatigue Life in HSLA Steels Welded Using the GMAW Process. *Metals* **2023**, *13*, 1910. https://doi.org/10.3390/met13111910

Academic Editor: Xudong Qian

Received: 26 September 2023
Revised: 15 November 2023
Accepted: 15 November 2023
Published: 20 November 2023

Copyright: © 2023 by the authors. Licensee MDPI, Basel, Switzerland. This article is an open access article distributed under the terms and conditions of the Creative Commons Attribution (CC BY) license (https://creativecommons.org/licenses/by/4.0/).

1. Introduction

The focus of the modern agricultural machinery industry is on economic gain and the greater structural optimization of its components to improve the quality of the final product and reduce maintenance costs [1,2]. To meet the growing demand of the agricultural industry, the metallurgical industry is developing modern structural steels with improved welding processing characteristics and mechanical property performance. Structural optimization and weight reduction are fundamental factors in ensuring competitiveness in the agricultural industry, achieving greater efficiency in their implements, and reducing environmental impact, including a decrease in CO_2 emissions during their application [1–4].

One of the most popular classes of structural steels is high-strength low-alloy (HSLA) steels, where the combination of alloying elements, processing, and heat treatment in recent decades has significantly evolved, enhancing the mechanical properties and toughness characteristics of these materials [2–4]. The fine microstructure and thermomechanical processing of HSLA steels, along with the addition of low-level alloy elements, result in the formation of fine precipitates and regions of carbide and nitride formation [5–7]. These intermetallic particles resulting from the mentioned alloying elements contribute to matrix reinforcement by impeding the movement of dislocations and promoting grain refinement [7–10]. The low carbon content in these materials, combined with the low quantity of alloying elements, makes the material easily weldable [11]. However, determining the appropriate welding technique and ideal process still poses challenges for welding engineers [12]. The steel in the presented study is LNE 600, which is used in the construction of lightweight and high-strength structures and equipment. This material is characterized by its high mechanical strength achieved through the addition of alloy elements such as

V, Ti, Nb, as well as Cr, Mo, and Ni, which, along with its manufacturing process, ensure its properties.

High-strength low-alloy steels exhibit high strength due to their microstructure, making them highly sensitive to welding processes [12,13]. Research related to the welding of high-strength low-alloy steels focuses on reducing hardness values in the Heat-Affected Zone (HAZ) compared to the base material. A region of lower hardness does not always indicate a reduction in the static strength of welded joints. The area of this low-hardness region and the alloying elements present in the welding consumables can ensure the mechanical strength in this region, even with microstructural modifications [12–17]. The region of lower strength in welded joints is typically in the recrystallized region of the heat-affected zone. The initiation of fatigue cracks is often observed near the edge of the weld bead on the face side, and in some cases, crack initiation is observed near the root of the joints [16,17].

Authors also report that the non-uniform cooling generated by welding HSLA steels can lead to cold cracks, reduced tensile strength, and areas of low hardness in the HAZ. This also indicates that the fatigue performance of HSLA welds is affected by the heterogeneities of the filler metal, regions of low hardness in the HAZ, and geometric factors that concentrate stresses [17–20]. In the study by Denisa et al. [20], fatigue tests were conducted on the Domex700 MC base material and the material welded with ER110S-G electrode. A decrease of 19.6% was observed in the hardness of the Heat-Affected Zone (ZTA) compared to the base metal, as well as a 12.8% reduction in fatigue load from the base material to the welded material. In the research by Stoschka et al. [21], which assessed the influence of filler metal and shielding gases on the fatigue life of HSLA (High-Strength Low-Alloy) materials, the geometric notch effect had the greatest impact on fatigue life behavior. Minimizing the notch resulted in a 70% increase in fatigue life, while variations in filler metal and shielding gas contributed only about 7% to the increase in fatigue life. In the studies presented by Ślęzak [1], which evaluated low-cycle fatigue tests on two different welded joints, V-shaped and square joints, the square joints exhibited slightly higher fatigue life when compared to the V-shaped joints. They also had higher hardness and a better hardness distribution. Hariprasath et al. [14] examined the effect of stress on the high-cycle fatigue behavior of HSLA welded joints. The results showed that the fatigue life of the welded joints was lower than that of the base material due to residual stresses and lower mechanical properties. Studies by Maurya et al. [22] indicate the importance of applying different compositions of filler metals in improving the mechanical resistance properties and fatigue life of joints. The addition of Ni to the weld metal has a positive impact on the tenacity of the joints and on solid solution hardening, leading to greater hardness and the greater formation of acicular ferrite, improving the tenacity of the joints. In this context, Moshtaghi et al. [23] indicated the benefits of reducing heat input on the mechanical properties of welded joints and the microstructural formation of the thermally affected zone.

The main objectives of this research are to evaluate the behavior of welds carried out using the GMAW process on LNE 600 steel; this study seeks to better understand the fatigue behavior of the joints in view of the premature failure of these components in agricultural implement applications. We investigated the influence of consumable electrodes applied in conjunction with shielding gases on the metallurgical transformations occurring in the Heat-Affected Zone (HAZ) of LNE 600 steel welded using the GMAW process. The tensile strength and fatigue resistance properties of the joints were also studied, including evaluations of locations where static and dynamic fractures occurred, as well as the assessment of fracture surfaces for the specimens subjected to fatigue testing.

2. Materials and Methods

2.1. Base Material

In this work, the LNE 600 steel (base metal), commercially known as NBR6656, which belongs to High-Strength Low-Alloy steel (HSLA), was selected as the study material. The LNE 600 steel is considered a high-strength, low-alloy steel due to the low levels of

alloying elements present in the material, along with its manufacturing process through controlled rolling with grain refinement, which allows the best properties of this material to be extracted, as represented in Figure 1a. In addition, the choice of LNE 600 steel was based on studying mainly in the HAZ. In Figure 1b, only LNE 380 steel is referred to as a structural reinforcement used in the agricultural implement. The chemical composition of the base material is presented in Table 1.

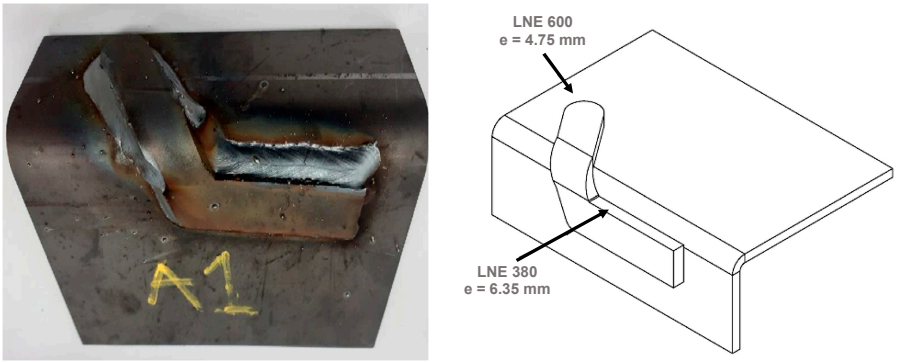

(**a**) (**b**)

Figure 1. (**a**) Segment of the agricultural implement and (**b**) diagram of the implement with its dimensions in millimeters.

Table 1. Chemical composition (wt%) of base metal, obtained using optical emission spectroscopy.

Material	C	Si	Mn	S	P	Al	Ni	Mo	Cu	W	N
Base Metal LNE 600	0.15	0.35	1.90	0.015	0.025	0.015%	4.95	2.74	0.29	0.054	0.225

Figure 2 shows the microstructure at different magnifications of LNE 600 steel, from which it is possible to observe a Ferritic–Pearlitic structure with carbide aggregates aligned along the rolling direction.

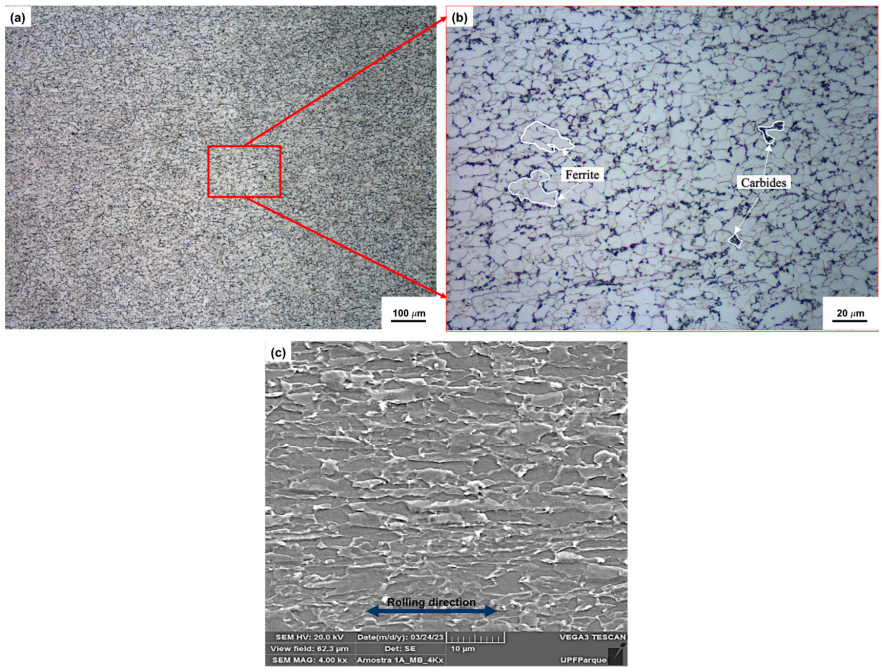

Figure 2. Microstructure of base material LNE 600. (**a**) Low-magnification optical image, (**b**) high-magnification optical image, and (**c**) high-magnification SEM image.

2.2. Welding Wire

The electrodes used in the welding were ER70S-6, ER110S-G, and ER120S-G, all with a diameter of 1 mm; these electrodes were selected to verify the application of the ER70S-6 electrode and its possible impacts on the properties of the joints. In contrast, the ER110S-G and ER120S-G electrodes were chosen due to their mechanical resistance after welding superior to the welding material. In addition, two shielding gases were used, Ar + 15% CO_2 and Ar + 5% O_2. The chemical composition and mechanical properties of the three welding consumables are listed in Tables 2 and 3, respectively.

Table 2. Chemical composition of welding wire (wt.%), obtained by the as-received wire.

Welding Wire	C	Si	Mn	S	P	Ni	Cr	Mo	Cu	N	V
ER70S-6	0.10	0.90	1.50	-	-	-	-	-	-	-	-
ER110S-G	0.06	0.6	1.6	0.01	0.01	1.4	0.3	0.25	0.07	0.25	0.07
ER120S-G	0.081	0.8	1.75	-	-	2.22	0.41	0.533	-	-	-

Table 3. Minimum mechanical properties that welds must present after welding.

Welding Wire	0.2% Yield Strength (MPa)	Ultimate Tensile Strength (MPa)	Elongation (%)
ER70S-6	470	560	26
ER110S-G	715	805	17
ER120S-G	920	940	18

2.3. Welding Process

Before welding, the oxide layer on the surface of the LNE 600 steel was removed using sandpaper. Metal residues and oil were removed with acetone. Then, they were dried immediately after ultrasonic washing with ethanol before starting the welding process. A butt joint was used for the non-beveled steel plates. During the welding process, the LNE 600 steel plates were fixed with a press system to minimize the deformation of the steel plates.

The welding process was carried out manually, using the Gas Metal Arc Welding (GMAW) process, using a SUMIG FALCOM 400 welding source with automatic feeding. The welding parameters applied were an alternating current of 220 A and a voltage of 22 V, with a constant shielding gas flow of 18 L/min.

2.4. Microstructural Characterization

The sequence of steps according to the ASTM E3-01 standard [24] was followed to carry out the microstructural analysis of the samples. First, the samples were cut with a refrigerated horizontal band saw. Next, they were mounted in Bakelite resin and subjected to a semi-automatic grinding process using silicon carbide sandpaper from Nº 80 to 1200. The samples were polished in two stages: first, a solution of alumina with a granulometry of 3 and 1 µm, and second, a suspension of colloidal silica for the final finish with particles of size 0.04 mm. All samples were etched with a 4% Nital solution for 10 s, after which the samples were immediately washed with water, followed by ethanol, and finally blown dry with hot air. The microstructural observation of the samples in the different areas of analysis was carried out using SEM scanning electron microscopy (Tescan USA, Vega 3 LM model) and an OM optical microscope (Zeiss Scope model A1).

2.5. Mechanical Properties

2.5.1. Microhardness Tests of Welds

Microhardness measurements were carried out to determine the different regions of analysis. This was evaluated using Vickers microhardness tests using a Shimadzu micro

durometer, Model HMV-G20ST. Indentations with a 0.2 mm indentation distance were made by applying a static load of 200 gf for 10 s at room temperature. Figure 3a,b) show the schematic of the regions measured starting from the center of the filler metal, traversing the Base Metal (BM), Fine-Grained Heat-Affected Zone (FGHAZ), Coarse-Grained Heat-Affected Zone (CGHAZ), and Filler Metal (FM).

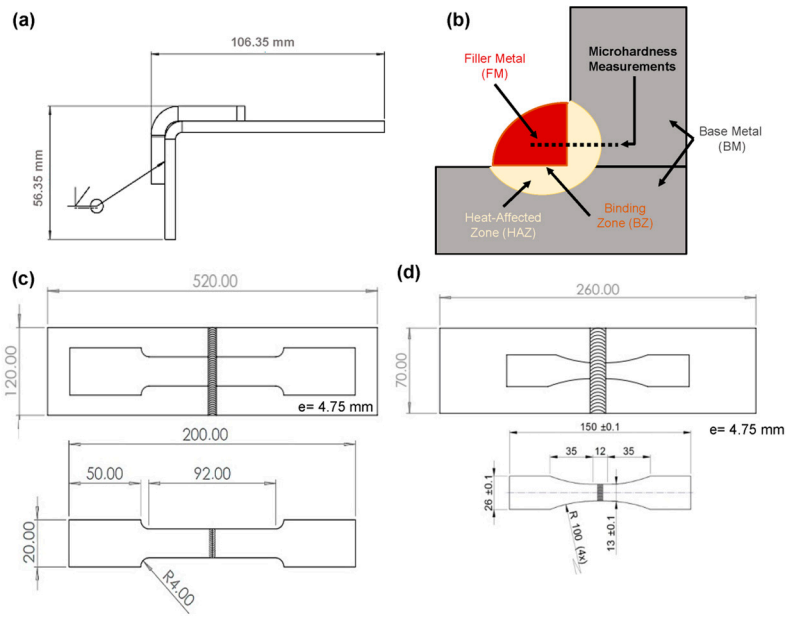

Figure 3. Schemes of mechanical characterizations for the LNE 600 steel. (**a**) Disposition of the test bodies, (**b**) measurement of microhardness of the analyzed regions, (**c**) dimensions of the specimens for the tensile test, and (**d**) dimensions of the specimens for the fatigue test.

2.5.2. Tensile Test

The tensile tests were carried out in accordance with the ASTM E8/E8M-22 standard [25] for manufacturing test pieces and the execution of tests. These tests were carried out using a Schenck universal testing machine, model UPM-200, and a constant strain rate of 0.5 mm/min was applied. In Figure 3c), a schematic is provided showing the welds' location and the specimens' subsequent machining. A total of 7 samples were carried out for each welding condition.

2.5.3. Fatigue Test

The different welding conditions were compared to evaluate the fatigue test following the ASTM 466-21 standard [26] guidelines. The tests were carried out using test loads at 50% and 60% of the tension, which were set at 620 MPa. A sanding process was carried out on the faces of the specimens using sandpaper with a number from 80 to 150 to eliminate burrs and reduce the stress concentration factor. These tests were carried out using the Shimadzu Servopulser model EHF–EV101 machine, applying loads axially at a frequency of 15 Hz and a load ratio of 10% ($R = F_{min}/F_{max} = 0.1$). The sample geometry is shown in Figure 3d).

3. Results and Discussion

3.1. Microstructure Characterization

3.1.1. Macrostructure of the Welded Joints

The butt-welding tests were carried out through the GMAW process and, in Figure 4a,b), the macrographs of the different zones in the cross-section of the base material (BM), heat-affected zone (HAZ), and the weld metal (FM), of the ER120S-G electrode using Ar + 5% O_2 gas and the ER70S-6 electrode using Ar + 15% CO_2 gas as shown, respectively. Additionally, Figure 4 indicates the different sizes in the HAZ widths (red arrows). The

welding procedures were performed satisfactorily, and the weld was free of welding defects, such as porosities, inclusions, cracks, voids, and other defects. However, small areas with a lack of fusion were observed that are common and susceptible in the GMAW process.

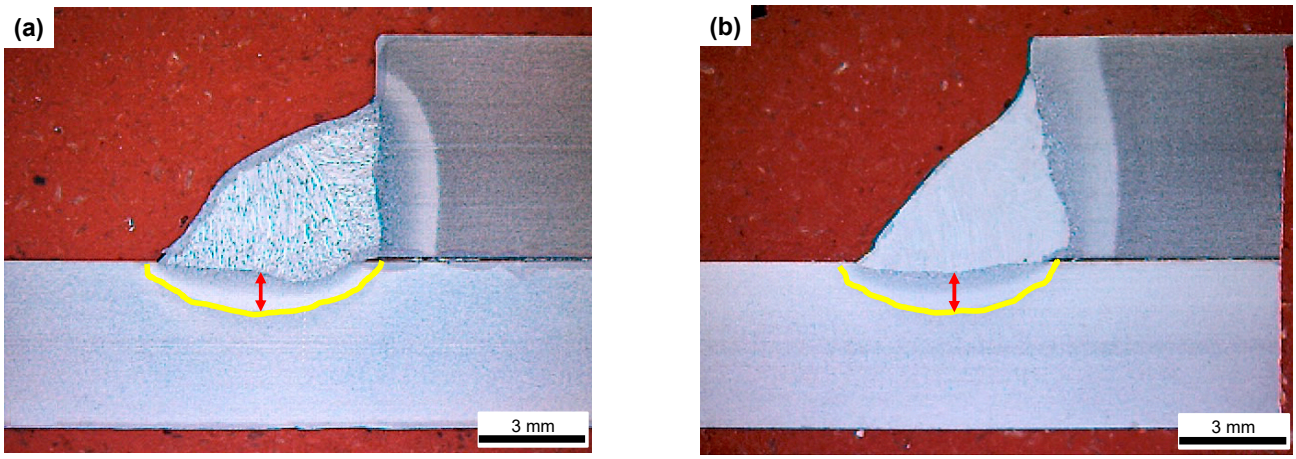

(**a**) (**b**)

Figure 4. Macrograph of the welded joints. (**a**) ER70S-6/Ar + 15% CO_2 and (**b**) ER120-G/Ar + 5% O_2.

The width of the HAZ was measured from the optical microscopy images, and its average values and standard deviation are presented in Table 4. The characteristics of the weld, such as the width of the HAZ and the width of the weld, are the key factors to estimate the quality of the weld. There is an increase in the HAZ width when using the ER70S-6 electrode compared to the other electrodes in terms of mean values. In general, for each electrode, increases in the width of the HAZ are observed when Ar + 15% CO_2 gas is used compared to Ar + 5% O_2 gas. It is observed that the ER120S-G electrode with Ar + 5% O_2 showed a smaller HAZ with an average of 1.11 mm in all electrode and gas combinations. However, if the error bars are analyzed, it can be seen that adding one standard deviation of the HAZ width of the ER120S-G electrode with Ar + 5% O_2 is almost equivalent to the average HAZ width of the ER110S-G electrode with Ar + 15% CO_2 subtracting one standard deviation. This analysis could suggest the high heat exchange capacity of CO_2 to transfer more significant heat to the base metal, and the difference between means could be due to random variability and/or the manual GMAW process.

Table 4. HAZ width for each electrode and gas used; the measurement region was indicated by arrows in the macrograph in Figure 4.

Average Dimensions of the HAZ (mm)		
Electrode	**Gas**	**Average Dimension (mm)**
ER70S-6	Ar + 15% CO_2	1.93 ± 0.43
	Ar + 5% O_2	1.82 ± 0.09
ER110S-G	Ar + 15% CO_2	1.71 ± 0.53
	Ar + 5% O_2	1.35 ± 0.07
ER120S-G	Ar + 15% CO_2	1.37 ± 0.05
	Ar + 5% O_2	1.11 ± 0.22

3.1.2. Microstructure of Heat-Affected Zone

Figure 5 shows the HAZ from coarse (CGHAZ) to more refined grains (FCHAZ) with 1000× magnification, using gas Ar + 15% CO_2. The region of the thermally affected zone for the ER70S-6 electrode presented a coarser microstructure, followed by ER110S-G and ER120S-G, which presented the most refined microstructure compared to the others. As the

weld solidifies and cools, the grains near the weld will become coarser, and the grains at the ends will be fine-grained, depending on the local cooling rate, which is determined by the alloy elements in the base material and welding parameters. Studies by Haupt et al. [27] on the geometric and microstructural evaluation of welds in high-strength steels applied in the agricultural industry demonstrated the same refining behavior and size of the HAZ. The classification of microstructures in the study by Thewlis et al. [28] was used to evaluate the morphology of phases generated in welds. It is possible to observe the similarity between the compositions and morphologies of the phases generated in the studies.

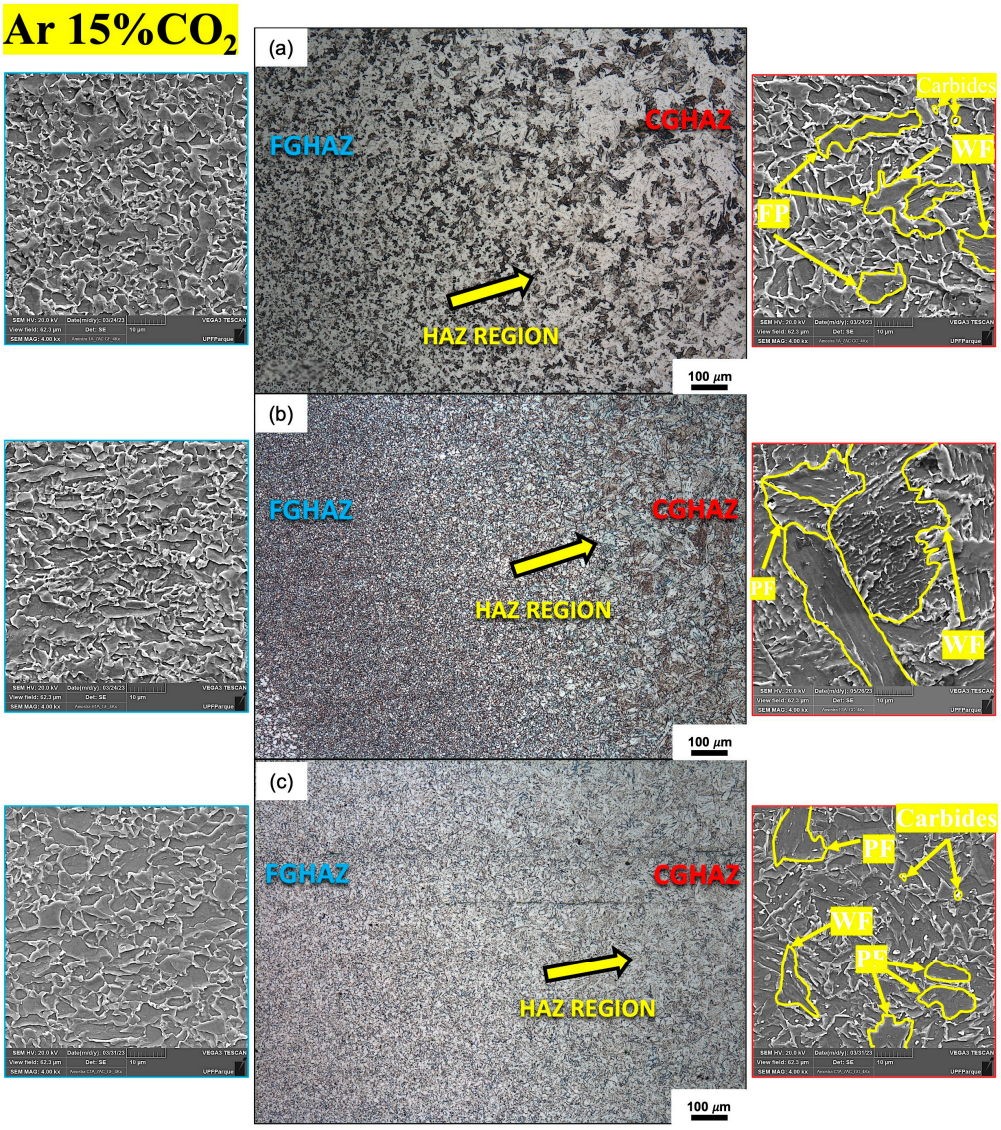

Figure 5. Microstructure of the samples using Ar gas + 15% CO_2 for the heat-affected zone (HAZ) region; transformation from coarse grain to refined grain. (**a**) ER70S-6; (**b**) ER110S-G; (**c**) ER120S-G. PF—Primary Ferrite; WF—Widmanstatten Ferrite.

Figure 6 shows the microstructure of the transition between the coarse- and fine-grain microstructures at higher magnifications ×4000 (SEM). Figure 6 shows that grain refinement in the HAZ occurs as it moves away from the heat input region. When comparing the images obtained between the two gases, it can be verified that, in welds where O_2 gas is used, it had a smaller effect on grain refinement in the modified microstructure region, in line with the results obtained using macrographic measurements (Figure 4), indicating less warming and changes in this area.

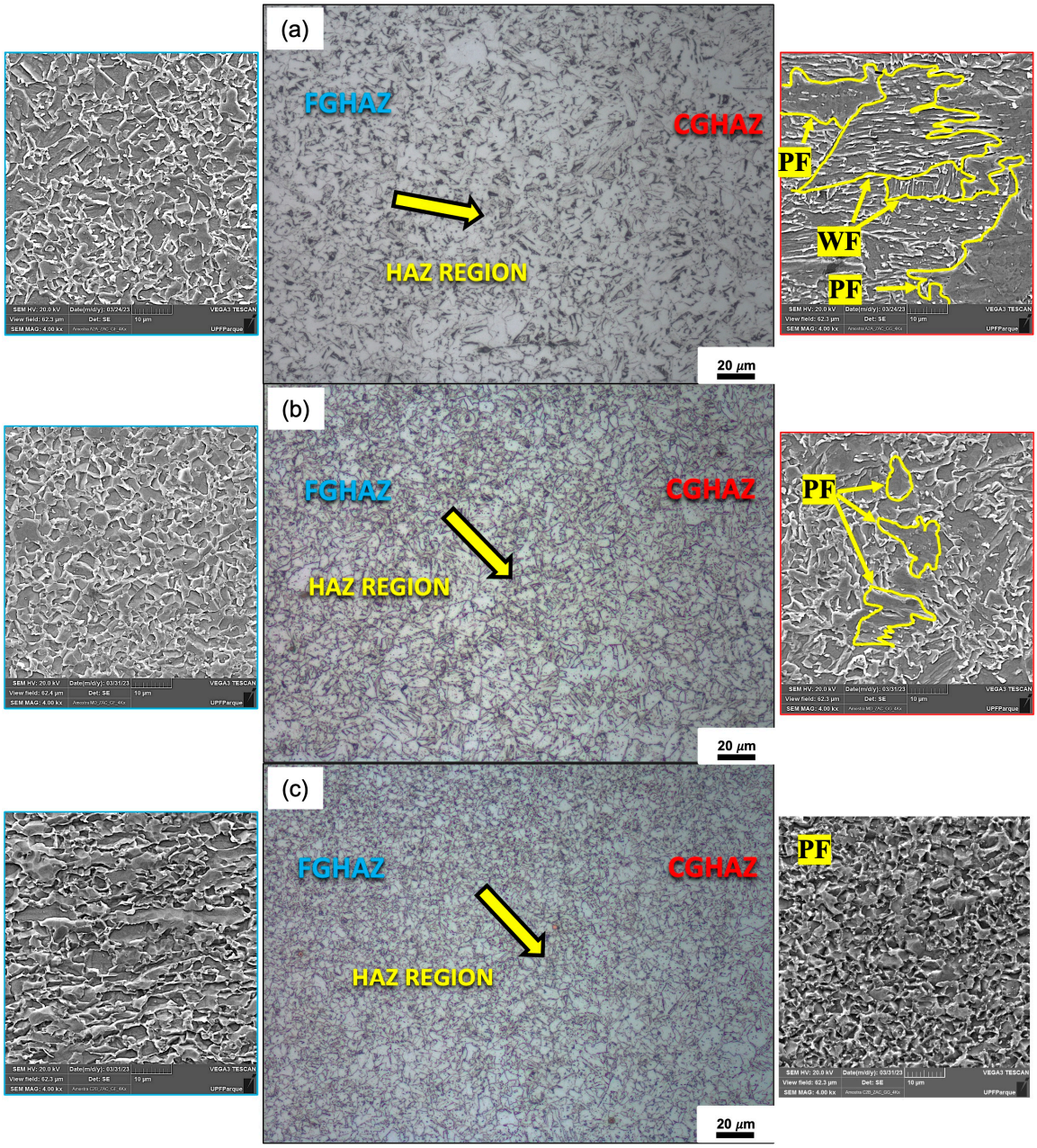

Figure 6. Microstructure of the samples using gas Ar + 5% O_2 for the heat-affected zone (HAZ) region; transformation from coarse grain to refined grain. (**a**) ER70S-6; (**b**) ER110S-G; (**c**) ER120S-G. PF—Primary Ferrite; WF—Widmanstatten Ferrite.

In both the welds made with O_2 and CO_2 gas, the micrographs showed similarity in the microconstituents. For the ER70S-6 electrode, both the O_2 and CO_2 welds presented formations of primary ferrite and Widmansttäten ferrite. In the study by Shi, Wang, and Ko [29], it is clear that the most frequent failures in welding are caused by excessive heat input, causing the production of Widmansttäten ferrite in the welded joint, affecting the plasticity of the joint. This resulted in the low toughness, decarburization, and softening of heat-affected areas.

In the ER110S-G electrode, also welded with both gases, the microconstituents found were primary ferrites. For the ER120S-G electrode, there was a more significant presence of primary ferrite compared to the other microconstituents, with primary ferrite being beneficial for the joint. According to the studies by Lee et al. [30], the primary ferrite is formed by a very fine needle-shaped ferrite and its orientation differs from that of the neigh-

boring sheets. The characteristics of acicular ferrite are widely recognized for their excellent combination of strength and toughness, thanks to its high internal dislocation density and high angle boundaries, which exhibit high resistance to cleavage crack propagation.

3.1.3. Microstructure of the Welding Wire

Figure 7 presents the microstructure of the main constituents found in the welding wire using shielding gas, Ar + 15% CO_2 and Ar + O_2, in the filler metal region using SEM. It is observed that the first column of Figure 7, using the shielding gas Ar + 15% CO_2, the filler metal region, using the ER70S-6 electrode, presented a less refined structure containing primary ferrite (PF) and regions with acicular ferrite (AF). The ER110S-G electrode showed the formation of PF and regions with AF. For the ER120S-G electrode, there was a more significant presence of AF compared to the others and little formation of PF, generating more excellent resistance in the region. In the case of the second column of Figure 7, which represents the use of the protective gas Ar + 5% O_2, PF, AF, and WF formations are identified for the ER70S-6 electrode. The ER110S-G electrode had a higher incident formation of PF and AF, highlighting that, in the ER120S-G electrode, it presents regions of mainly (AF) and parts with (WF).

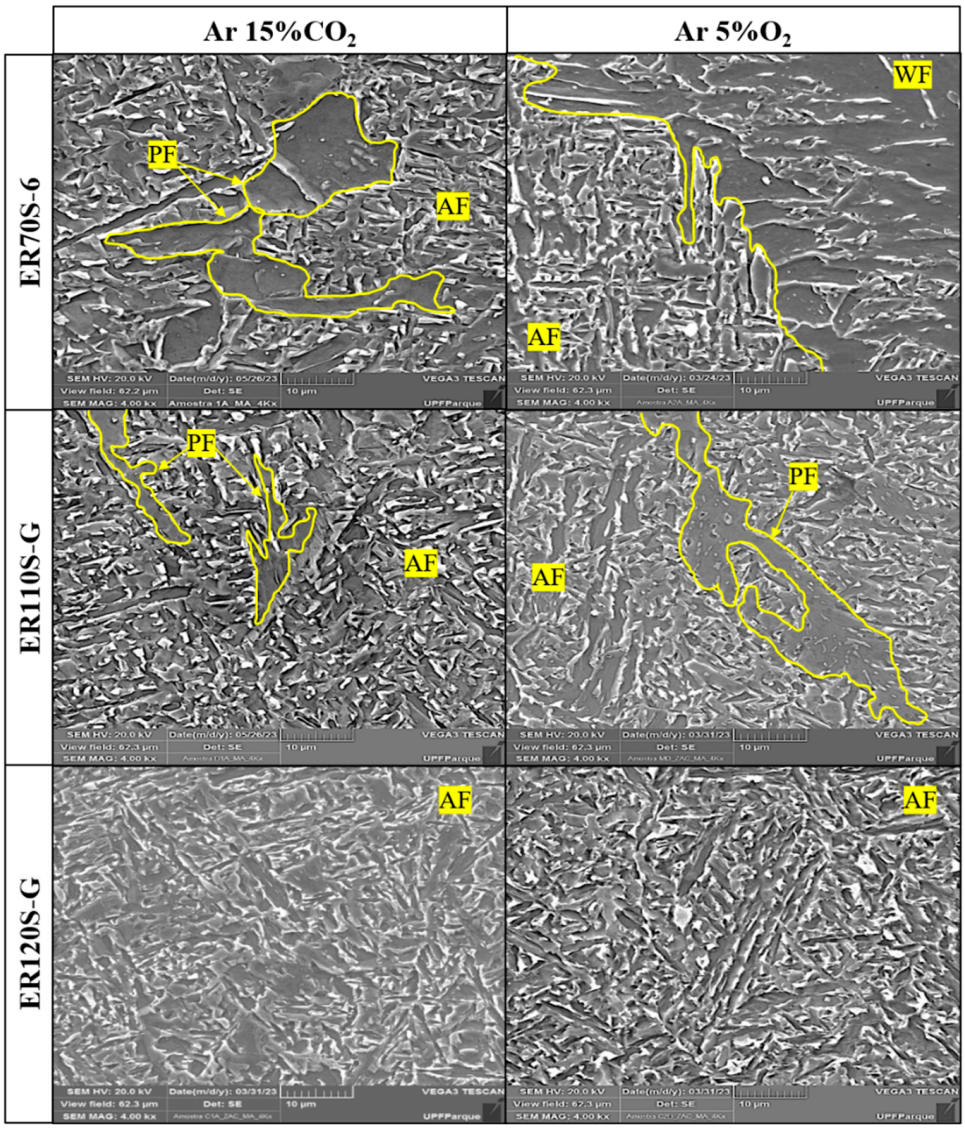

Figure 7. Region of the weld wire in welds performed with gas Ar + 5% O_2 e Ar + 15% CO_2. For the electrodes ER70S-6, ER110S-G, and ER120S-G. AF—Acicular Ferrite; PF—Primary Ferrite; WF—Widmanstatten Ferrite.

The microstructures in Figure 7 depend mainly on the chemical composition (Table 2), the heat input, and the cooling rate [29,31]. The chemical composition of the welding wire for the butt joint of the plates will have a final microstructure composed of the ferrite grain boundary (GBF), dendritic WF, PF, AF, and other microphases. Furthermore, during the cooling of the weld wire, the decomposition of austenite to ferrite begins at the above austenitic grain boundaries, and GBF will nucleate along the austenite grain boundaries and grow through the diffusion mechanism. Furthermore, as the temperature decreases, diffusion becomes slow, and WFs nucleate through a displacement mechanism; with continued cooling to lower temperatures, AF will nucleate intragranular inclusions [30].

On the other hand, the mechanical properties (Table 3) of the filler metals generate lower strengths in more significant AF, WF, and AF regions in the columnar region due to the higher cooling rate after welding. On the contrary, PF predominates in the overheated region. The decrease in cooling rate caused by preheating generated the conditions for forming this PF phase at the austenite grain boundary.

3.2. Microhardness Tests of Samples

The microhardness profiles for different welding conditions are presented in Figure 8a,b for different shielding gases. Additionally, Table 5 shows the average microhardness and standard deviation for each sample. For both Ar + 5%O_2 and Ar + 15%CO_2 gases, no significant differences were observed in the hardness results considering the standard deviations when the samples in each analysis region were globally compared. The graphs show the variation in the microhardness values starting from the base material and passing through the HAZ and weld metal regions, as indicated on the graphs. On the other hand, higher hardnesses occur in the weld metal areas for welding conditions with ER110S-G and ER120S-G electrodes. This is mainly due to the difference in microstructure evolution discussed in the previous section.

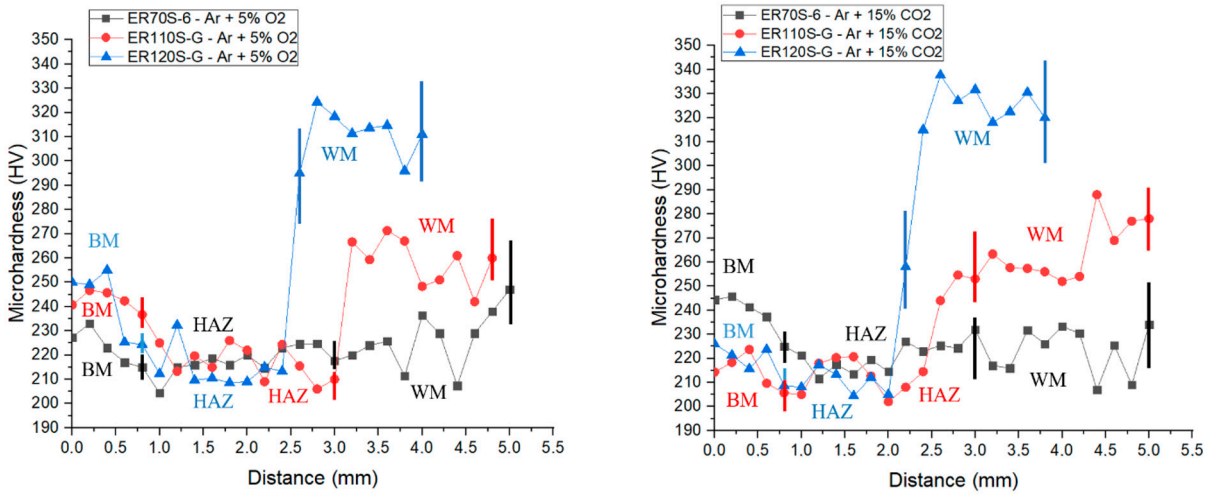

Figure 8. Microhardness for samples. (**a**) Ar + 5% O_2 and (**b**) Ar + 15% CO_2.

Table 5. Vickers microhardness of samples.

Samples	Ar + 5% O_2			Samples	Ar + 15% CO_2		
	BM	**HAZ**	**WM**		**BM**	**HAZ**	**WM**
ER70S-6	223 ± 21	217 ± 10	224 ± 14	ER70S-6	239 ± 17	221 ± 15	225 ± 13
ER110S-G	242 ± 21	218 ± 11	260 ± 12	ER110S-G	214 ± 21	215 ± 11	260 ± 13
ER120S-G	241 ± 17	219 ±21	313 ± 20	ER120S-G	219 ± 12	215 ± 18	325 ± 22

For a more accurate data assessment, a statistical analysis of the different regions of the welds was conducted, with the presentation of the data in Table 6 indicating whether there was a significant difference or not for the different regions of the welds. In the refined-grain region (FGHAZ), the lowest average hardness found was 211 HV for the ER120S-G electrode with Ar + 5% O_2, and the highest average hardness for this region was 218 HV for the ER70S-6 electrode using Ar + 5% O_2. There was no statistical difference between the samples in this region. The coarse-grain region (CGHAZ) exhibited the lowest average hardness with the ER110S-G + 15% CO_2 electrode at 214 HV, and the highest hardness with the ER120S-G electrode using Ar + 15% CO_2 with an average of 241 HV in this region. Similarly, there were no significant hardness differences in this region among the samples. For the weld metal region (WM), the electrode that showed the highest average hardness was the ER120S-G with Ar + 15% CO_2, with a hardness of 325 HV. The lowest average hardness was found for the ER70S-6 electrode with Ar + 5% O_2, measuring 224 HV. The gases used did not exhibit significant relevance in hardness.

Table 6. Tukey test for microhardness in different regions of samples.

Comparative Areas Tukey Test (Y = Yes and N = No)			
Weld Metal and Gas	**Result by Area**		
	CGHAZ–FGHAZ	**WM–FGHAZ**	**WM–CGHAZ**
ER70S-6–Ar + 5% O_2	N	N	Y
ER110S-G–Ar + 5% O_2	N	Y	Y
ER120S-G–Ar + 5% O_2	N	Y	Y
ER70S-6–Ar + 5% CO_2	N	N	N
ER110S-G–Ar + 5% CO_2	N	Y	Y
ER120S-G–Ar + 5% CO_2	N	Y	Y

As mentioned by Ngoula et al. [32] and Hariprasath et al. [14], acicular ferrite morphologies provide improved strength and toughness properties in welded joints. In the case of the ER120S-G electrode, it exhibited a higher formation of acicular ferrite, followed by ER110S-G, while ER70S-6 showed a lower formation, which explains the difference in hardness between the electrodes. Another factor that may influence the results was concluded by Gordon et al. [33] indicating that, for HSLA steels, the heat input ends up impacting hardness, with higher and more uniform hardness observed at low heat input levels. In the studies by Ribeiro et al. [34], regarding the morphologies of acicular ferrite, Widmanstätten ferrite, and grain boundary ferrite, they exhibited an average hardness of 250 HV with a standard deviation of ±10 HV. These results are consistent with the findings in the current study, both in terms of the identified microconstituents and hardness, which can also be related to the varying amounts of acicular ferrite found in the different electrodes, with this microconstituent having the highest hardness.

3.3. Tensile Tests

The results of the tensile tests of the samples are presented in Table 7. The standard deviation of each of the samples is shown. Overall, the Yield Strength and Maximum Stress were higher than the base metal. More specifically, the Yield Strength and Maximum Stress of the sample ER70S-6 Ar + 15% CO_2 presented values that were not significantly different from the base metal, considering the standard deviations.

Table 8 presents the results of Tukey's statistical tests for yield strength, tensile strength, and deformation recorded in the tests. For the yield limit results, it was possible to observe the best performance for the ER120S-G with CO_2 gas, ER120S-G with O_2 gas, and ER110S-G, with all these conditions composing Group A. The ER110S-G conditions with CO_2 gas and with the ER70S-6 electrode for both gas conditions showed inferior performance. In relation to the ultimate tensile strength, there was superior performance for the ER120S-G in the CO_2 gas condition, making up group A, the ER110S-G and ER120S-G electrodes with O_2 gas showed average behavior making up the AB group, while the electrode ER70S-6 with

O_2 application made up group B and the worst condition was the ER70S-6 electrode with Ar + 15% CO_2 gas. The deformation values did not show significant differences between the different welding conditions, all of which made up the same group A.

Table 7. Tensile test results for samples.

Weld Metal	Gas	Yield Stress (MPa)	Maximum Stress (MPa)	Strain (%)
Material Base	-	570 ± 33.4	640 ± 32.1	18.33 ± 0.62
ER70S-6	Ar + 15% CO_2	550 ± 29.4	619 ± 21.5	15.23 ± 1.54
	Ar + 5% O_2	601 ± 44	699 ± 10.1	13.95 ± 2.7
ER110S-G	Ar + 15% CO_2	638 ± 28.9	712 ± 25.6	18.19 ± 1.13
	Ar + 5% O_2	605 ± 26.3	702 ± 14.4	17.18 ± 1.02
ER120S-G	Ar + 15% CO_2	680 ± 5.3	753 ± 11	15.83 ± 2.47
	Ar + 5% O_2	649 ± 26.9	706 ± 16.4	16.12 ± 1.33

Table 8. Tukey test results for tensile testing of samples.

Tukey Test Yield Strength (MPa)				Tukey Test Tensile Strength (MPa)				Tukey Test Strain (%)			
Process	N	Mean	Grouping	Process	N	Mean	Grouping	Process	N	Mean	Grouping
ER120S-G (CO_2)	3	679.79	A	ER120S-G (CO_2)	3	753.01	A	ER110S-G (CO_2)	3	18.19	A
ER120S-G (O_2)	3	649	A	ER110S-G (O_2)	3	712.2	AB	ER110S-G (O_2)	3	17.18	A
ER110S-G (CO_2)	3	637.5	A	ER120S-G (O_2)	3	706	AB	ER120S-G (O_2)	3	16.12	A
ER110S-G (O_2)	3	605.3	AB	ER110S-G (CO_2)	3	701.67	B	ER120S-G (CO_2)	3	15.83	A
ER70S-6 (O_2)	3	601	AB	ER70S-6 (O_2)	3	699.33	B	ER70S-6 (CO_2)	3	15.23	A
ER70S-6 (CO_2)	3	550.1	B	ER70S-6 (CO_2)	3	618.6	C	ER70S-6 (O_2)	3	13.95	A

From the tensile test results, it is possible to observe that the use of the ER70S-6 electrode leads to a reduction in tensile strength values, with fractures occurring in the HAZ of the joints for this welding condition. In contrast, the other electrodes exhibited fractures in the base material region, since the yield stress and maximum stress values are higher than the base material. This factor can be attributed to some variation in mechanical properties in the base material combined with residual stresses and the application of higher resistance electrodes that modified the local residual stress conditions, indicating higher strength in the welded region. This is attributed to the higher content of alloying elements present in the ER110S-G and ER120S-G electrodes. In the tests conducted in this study, failures also occurred in the HAZ, with all tests using an Ar + 5% O_2 gas mixture and only one welded sample using the ER70S-6 electrode with an Ar + 15% CO_2 gas mixture. In the remaining cases, the rupture occurred in the base metal. According to Hariprasath et al. [35], these sample failures in the tensile test are due to elastic deformations and distortions in the heat-affected region. The residual strength state of the welds can affect the mechanical strength of the material, including the higher content of alloying elements and residual stress, can modify the mechanical strength conditions in materials. It is also noted by Kim, Hwang [36], in their studies, that the deformation is not uniform between the welded joint and the base material, with the joint and the HAZ having lower yield strength. In cases where parallel welds are made, with a 0° angle between the weld bead and the load axis, both the base material and the weld will be exposed to the same deformations, and the failure will occur in the region with lower ductility, typically the weld and HAZ. This aspect is also confirmed in the tensile tests conducted. The strain values showed no statistically significant differences, indicating the good ductility of the welded materials.

3.4. Fatigue Tests

Figure 9 presents the results of the fatigue tests conducted using the Ar + 5% O_2 gas and the electrodes. By evaluating the results, it is possible to observe a superior fatigue performance for the ER120S-G electrode under both load conditions employed in the tests. Following that, we can observe a moderate behavior for the ER110S-G electrode and an inferior performance for the ER70S-6 electrode across all fatigue load conditions. This behavior indicates the beneficial effect of the alloying elements present in the ER110S-G and ER120S-G electrodes, an effect that is also reported in other studies [1–3,6].

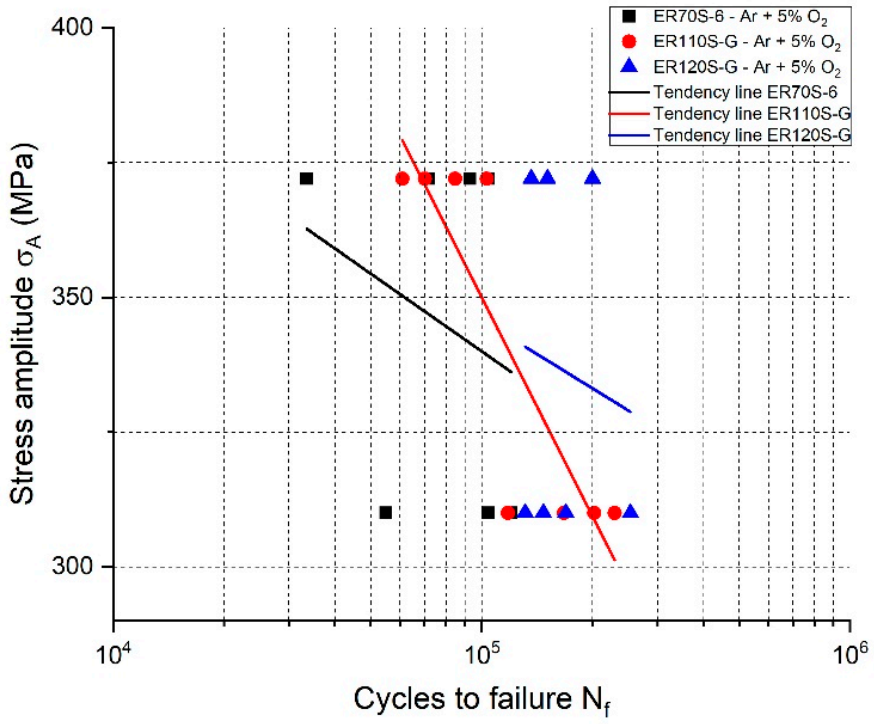

Figure 9. Trend line graph based on fatigue tests using Ar + 5% O_2 gas.

The trend lines presented in the graphs in Figure 9 indicate the superior fatigue behavior of the ER 120S-G electrode at both low and high loads, with the ER 110S-G electrode showing a similar performance at low loads. From this analysis, it is possible to verify the greater resistance to crack propagation generated by the ER 120S-G electrode with the use of O_2 gas, these benefits being combined with the reduction in the heat input generated by the shielding gas and the presence of alloy elements in the electrode, with the microstructure generated in this condition being the one with better quality and less modification compared to other conditions. The ER 70S-6 electrode presented a lower performance, as shown in the trend line in the graph; this fact is due to the worse microstructural conditions together with the higher incidence of defects for this welding condition.

In Figure 10, the graph with trend lines for the fatigue tests conducted with Ar + 15% CO_2 gas is presented. For the 60% load condition, unlike the results with the other gas, the ER70S-6 electrode exhibited the best fatigue performance, followed by the ER120S-G and ER110S-G electrodes. For the 50% load condition, the best performance was observed for the ER120S-G electrode, followed by the ER110S-G electrode, and the worst performance was recorded for the ER70S-6 electrode. This inferior performance under certain load conditions, shown by electrodes with high levels of alloying elements like the ER110S-G and ER120S-G electrodes, can be attributed to the geometric condition of the weld bead edge, which may result in potential geometric defects that enhance stress concentration in this region. Studies by Moravec et al. [15] and Rariprasath et al. [35] report the effect of stress concentrators at the edges of weld beads on the fatigue life of HSLA steels, indicating

that these points are severe stress concentrators due to the margin geometry. Along with the microstructural changes caused by heat in the Heat-Affected Zone (HAZ) that lead to local hardness reduction, these factors facilitate the initiation and propagation of cracks under cyclic loads.

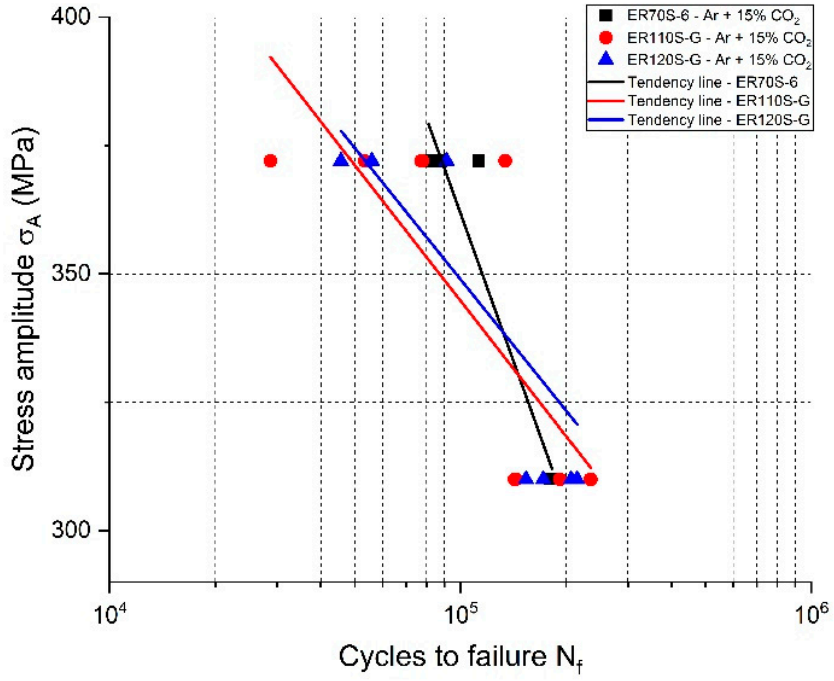

Figure 10. Trend line graph based on fatigue tests using Ar + 15% CO_2 gas.

The trend lines presented in Figure 10 indicate the fatigue behavior of the materials; in this sense, it is possible to evaluate a greater inclination for the ER 110S-G and ER 120S-G electrodes. This behavior is attributed to the more excellent resistance to the propagation of cracks at higher loads. Also, there is a significant difference in the number of cycles for loads of 60 and 50% concerning the maximum static voltage. The ER 70S-6 electrode showed better fatigue behavior for loads of 60% of the maximum voltage and fatigue life, similar to the other electrodes for loads of 50%; this factor indicates greater difficulty in opening cracks in this welding condition.

Tables 9 and 10 present the fatigue cycles with the standard deviation after tests, and the Tukey statistical test results for assessing fatigue behavior until failure. It is observable that the best fatigue life performance is achieved with the use of O_2 gas for the ER120S-G electrodes, followed by the ER110S-G electrode, with inferior performance for the ER70S-6 electrode. The Tukey statistical test was evaluated for the two load levels, 60% and 50%. For the 60% load condition, the best performance was observed for the welding condition using the ER120S-G electrode with O_2 gas, followed by a second group comprising the other analyzed conditions. The Tukey test for the 50% load condition revealed the presence of three distinct groups. Group A consisted of the ER110S-G electrode with Ar + 15% CO_2 gas, followed by group AB with the ER120S-G, ER70S-6, ER110S-G, and ER120S-G electrodes. The condition showing the poorest performance was ER70S-6 with O_2 gas.

The behavior observed for all welding conditions shows points with relatively high standard deviation, and the results presented are very susceptible to the formation of the margin of the beads as points of crack nucleation, to the presence of residual stresses arising from the cooling of the welded joints, and are also related to the presence of inclusions and a lack of fusion as main welding defects that can contribute to the reduction in fatigue life. The results found in this study indicate the beneficial effect of the alloying elements present in the addition electrodes, but they also reinforce the hypothesis that the geometric factors

of the welding bead must be correctly controlled together with the heat generated during welding and the residual stresses under penalty of reduced fatigue life.

Table 9. Fatigue life results for the different welding conditions.

		Condition Shielding Gas O_2	
Weld Metal	**Tensile (MPa)**	**Average Fatigue Cycles (Nf) * 10^3**	**Standard Deviation**
ER70S-6	372	75.6	31.14
	310	93.2	34.11
ER110S-G	372	79.8	18.46
	310	179.32	48.19
ER120S-G	372	162.36	33.31
	310	175.25	54.4
Condition Shielding Gas CO_2			
ER70S-6	372	91.45	14.54
	310	181.06	1.40
ER110S-G	372	74.34	39.16
	310	189.77	45.84
ER120S-G	372	64.26	23.95
	310	187.01	28.84

Table 10. Tukey test for fatigue life across the different welding conditions.

Tukey Test Fatigue 60%				**Tukey Test Fatigue 50%**			
Process	**N**	**Mean**	**Grouping**	**Process**	**N**	**Mean**	**Grouping**
ER120S-G (O_2)	4	162,361	A	ER110S-G (CO_2)	4	189,768	A
ER70S-6 (CO_2)	4	91,448	B	ER120S-G (CO_2)	4	187,015	AB
ER110S-G (O_2)	4	79,806	B	ER70S-6 (CO_2)	4	181,063	AB
ER70S-6 (O_2)	4	75,603	B	ER110S-G (O_2)	4	179,326	AB
ER110S-G (CO_2)	4	74,340	B	ER120S-G (O_2)	4	175,254	AB
ER120S-G (CO_2)	4	64,260	B	ER70S-6 (O_2)	4	93,204	B

Fractographic Analysis of Fatigue Tests

For the fractographic analysis of the samples welded with different filler electrodes and 5% O_2 gas, images of the fracture surface are shown using a SEM. The images are presented in Figure 11, with magnifications of 20×, 500×, and 20k× applied to identify cracks fatigue initiation, propagation regions and fatigue streaks (FS red arrows) were discovered. Defects such as a lack of fusion and inclusions, indicated by arrows in the images, can be observed, with cycle marks also shown for the 20k× magnification. Through the analysis of fracture surfaces, it becomes evident that defects like a lack of fusion, inclusions, and weld toe effects are the main points of failure initiation. The fracture behavior was ductile, suggesting that the material did not exhibit areas of high hardness leading to embrittlement, and fatigue fracture was accelerated by the presence of defects and areas of reduced hardness microstructure in the Heat-Affected Zone (HAZ) of the welded materials, allowing the progression of cracks.

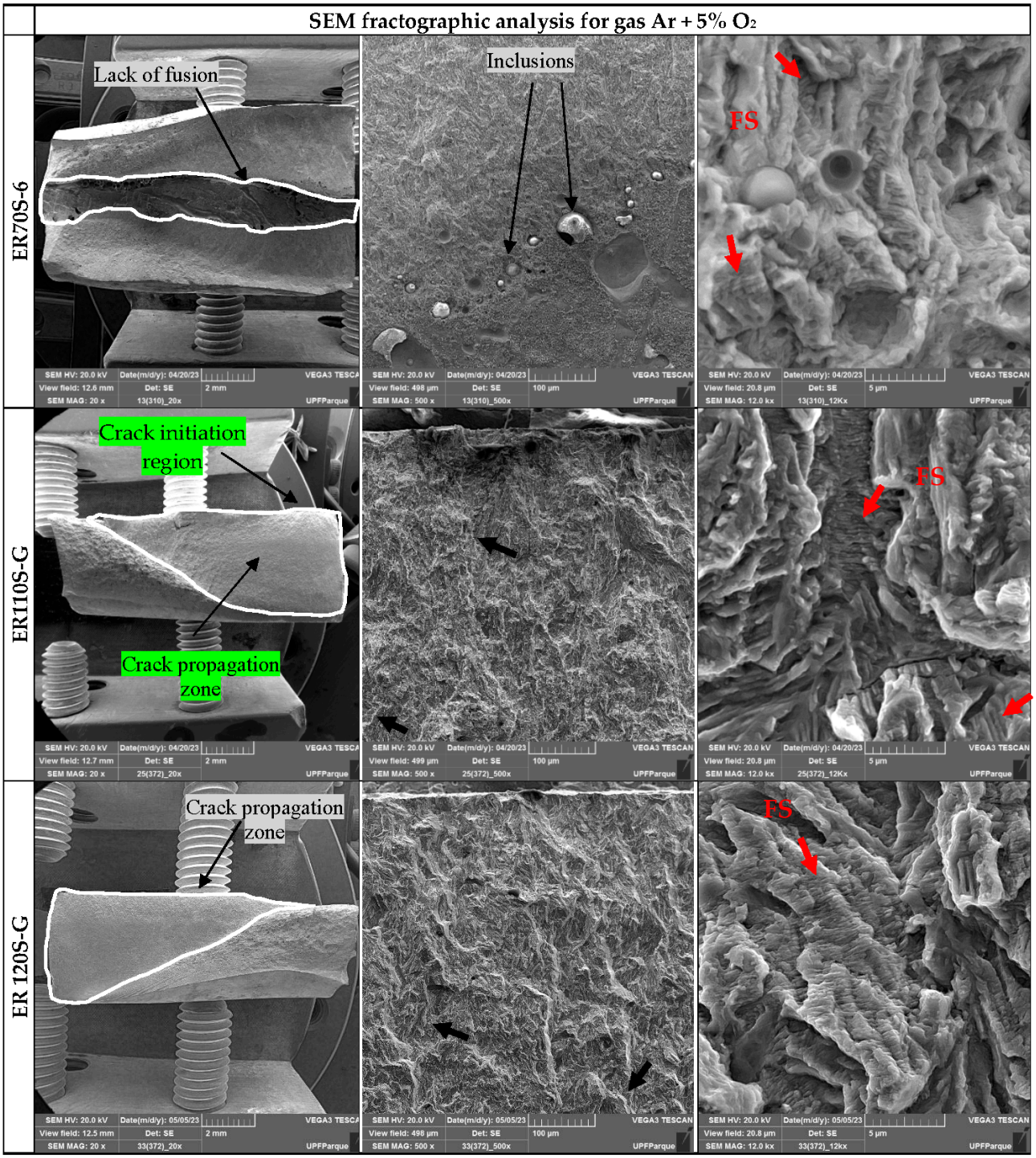

Figure 11. SEM fractographic analysis for the samples using Ar + 5% O_2 gas.

The images presented in Figure 12 display the fracture surfaces for the different deposition electrodes using Ar + 15% CO_2 gas. In this case, upon assessment, no defects, such as inclusions, porosities, or a lack of fusion, were recorded for the samples. This indicates the better protection and fusion capabilities for this shielding gas. The cracks initiated at the edges of the deposited weld beads exhibited slow propagation, culminating in a ductile final fracture.

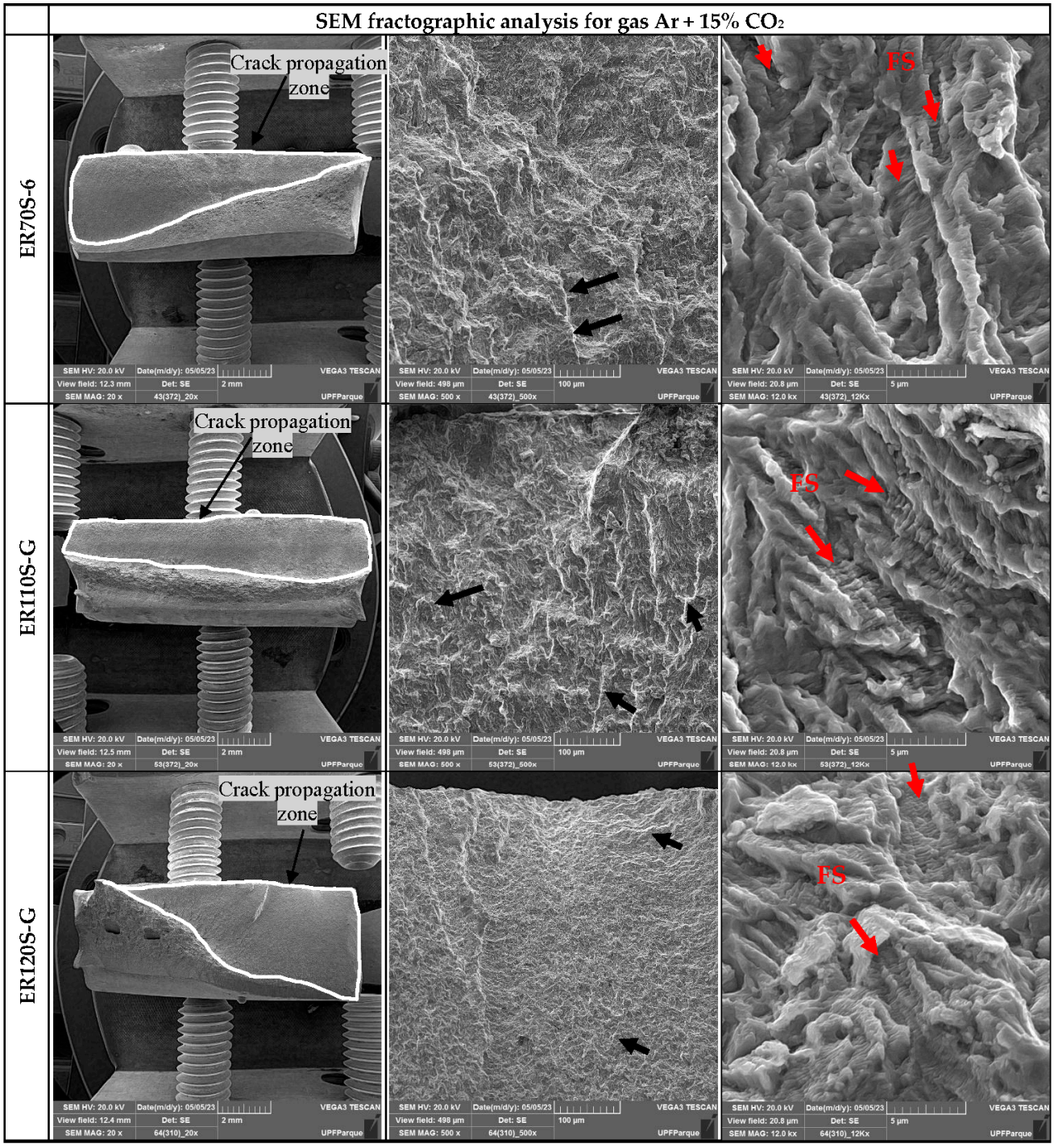

Figure 12. SEM fractographic analysis for the samples using Ar + 15% CO_2 gas.

The envelopes marked in Figures 11 and 12 (20×) indicate the areas of fatigue cracking. Both Figures are characterized by a very diverse morphology and a system of numerous origins of fatigue cracks. The photographs in Figures 11 and 12 (500×) show the areas of stable crack growth at a very close distance from the initiators.

The ductile character of cracking is preserved in the initial cracking stage and during stable growth. The most visible differences in the fracture surface images are the less crushed areas in the ER120S-G Ar + 15% CO_2 sample resulting from small surface deformations in the compression phase of the load. In general, cracking is accompanied by numerous secondary cracks, which are indicated by the arrows. Fatigue streaks (red

arrows) were also discovered, which appear frequently (20k×), although in many cases they have been crushed (ER70S6).

4. Discussion of Results

The welding performed under different electrode compositions and gases allowed us to observe that the HAZ sizes varied depending on the use of different electrodes and gases. This indicates that the combination of the ER120S-G electrode and Ar + 5% O_2 gas proved to be the most suitable choice in terms of HAZ size and microstructural quality. It exhibited a predominant microstructure of acicular ferrite in the fused region of the joints and an HAZ with fewer microstructural modifications and a smaller heat-affected area.

The microhardness values were higher in the fused zone region for the ER110S-G and ER120S-G electrodes due to the greater quantity of alloying elements present in these electrodes and the formation of acicular ferrite microstructures in the fused region of these electrodes. It was also possible to observe a better static performance for the joints obtained with the ER110S-G and ER120S-G electrodes, indicating the higher mechanical strength resulting from the addition of alloying elements by the filler wire.

The fatigue life of the joints was superior in the ER120S-G welding condition with the use of O_2 gas, closely followed by the ER110S-G electrode condition. This suggests that crack propagation was slower due to the finer microstructure present in these welding conditions. Crack nucleation primarily occurred at the edges of the deposited weld beads for most of the fatigue conditions, indicating that geometric factors and welding defects, such as inclusions and a lack of fusion, were predominant in crack initiation. The crack propagation was slow due to the high ductility of the materials evaluated.

5. Conclusions

There was a reduction in the size of the HAZ for the ER120S-G electrode with O_2 gas compared to the other evaluated conditions. For the ER70S-6 and ER110S-G electrodes, the smaller HAZ occurred when using Ar + 15% CO_2 gas.

The microstructural analysis indicated a smaller modification of the HAZ microstructure when the ER110S-G and ER120S-G electrodes were applied together with the Ar + 5% O_2 gas.

The microstructural analysis indicated a finer grain refinement in the HAZ for the ER110S-G and ER120S-G electrodes, with a predominance of acicular ferrite in both welds. This microstructure is beneficial for mechanical strength.

Regarding the microhardness tests, there was an increase in the hardness values in the filler wire region for all ER110S-G and ER120S-G electrodes. The HAZ region exhibited a reduction in the hardness values for all evaluated conditions, with hardness significantly differing in comparison to the filler wire region.

The tensile strength of the joints was adequate for most of the evaluated conditions, with the exception being the ER70S-6 welding condition with Ar + 5% O_2 gas. In fatigue, the welding condition with the ER120S-G electrode and Ar + 5% O_2 gas showed the best overall performance, while the other load conditions and electrodes were statistically similar.

The fatigue cracks initiated near the edge of the weld bead, and their propagation was controlled by the microstructural condition of the HAZ in different joints and welding defects present in the crack initiation region.

It was possible to observe a stable propagation of fractures with a large area, culminating in a final fracture with a ductile mode. This indicates the high ductility of the material in the crack propagation region.

The fatigue results indicate the benefits of applying O_2 gas together with electrodes with higher contents of alloy elements such as ER110S-G and ER120S-G.

Author Contributions: Conceptualization, F.B., H.S.Z., R.I.A. and W.H.; Methodology, F.B., H.S.Z. and W.H.; Validation, F.B. and W.H.; Formal analysis, F.B., H.S.Z., R.I.A. and W.H.; Investigation, H.S.Z.; Data curation, H.S.Z. and R.I.A.; Writing—original draft, F.B., H.S.Z., R.I.A. and W.H.; Writing—review and editing, F.B. and W.H.; Supervision, F.B. All authors have read and agreed to the published version of the manuscript.

Funding: This research received no external funding, and the APC was funded by the Pontificia Universidad Católica de Valparaíso (PUCV).

Data Availability Statement: The raw data required to reproduce these findings are available and can be used with prior authorization from the authors. Contact francisco.briones@pucv.cl for more information.

Conflicts of Interest: The authors declare no conflict of interest.

References

1. Ślęzak, T. Fatigue examination of HSLA steel with yield strength of 960 MPa and its welded joints under strain mode. *Metals* **2020**, *10*, 228. [CrossRef]
2. Mičian, M.; Harmaniak, D.; Nový, F.; Winczek, J.; Moravec, J.; Trško, L. Effect of the t 8/5 Cooling Time on the Properties of S960MC Steel in the HAZ of Welded Joints Evaluated by Thermal Physical Simulation. *Metals* **2020**, *10*, 229. [CrossRef]
3. Gáspár, M. Effect of welding heat input on simulated HAZ areas in S960QL high strength steel. *Metals* **2019**, *9*, 1226. [CrossRef]
4. Jiménez-Peña, C.; Goulas, C.; Preubner, J.; Debruyne, D. Failure mechanisms of mechanically and thermally produced holes in high-strength low-alloy steel plates subjected to fatigue loading. *Metals* **2020**, *10*, 318. [CrossRef]
5. Barbaro, F.; Kuzmikova, L.; Zhu, Z.; Li, H. Weld Haz Properties in Modern High Strength Niobium Pipeline Steels. In Proceedings of the Energy Materials 2014, Xi'an, China, 4–6 November 2014; Springer International Publishing: Cham, Germany, 2016; pp. 657–664.
6. Schaupp, T.; Schroepfer, D.; Kromm, A.; Kannengiesser, T. Welding Residual Stresses in 960 MPa Grade QT and TMCP High-Strength Steels. *J. Manuf. Process.* **2017**, *27*, 226–232. [CrossRef]
7. Branco, R.; Berto, F. Mechanical Behavior of High-Strength, Low-Alloy Steels. *Metals* **2018**, *8*, 610. [CrossRef]
8. Laitila, J.; Larkiola, J. Effect of Enhanced Cooling on Mechanical Properties of a Multipass Welded Martensitic Steel. *Weld. World* **2019**, *63*, 637–646. [CrossRef]
9. Njock Bayock, F.; Kah, P.; Mvola, B.; Layus, P. Effect of Heat Input and Undermatched Filler Wire on the Microstructure and Mechanical Properties of Dissimilar S700MC/S960QC High-Strength Steels. *Metals* **2019**, *9*, 883. [CrossRef]
10. Ke, L.; Li, Y.; Chen, Z.; Feng, Z.; Yan, B.; Zhu, F.; Yuan, P. Effect of microstructure on fatigue crack growth behavior of surface- and middle-layer materials of thick high-strength bridge steel plates. *Fatigue Fract. Eng. Mater. Struct.* **2023**, *6*, 485–500. [CrossRef]
11. Zhou, S.; Shen, Z.X.; Wang, L.; An, J. Study of overloading retardation on fatigue crack propagation behavior in 300M steel. *Fatigue Fract. Eng. Mater. Struct.* **2022**, *45*, 3288–3301. [CrossRef]
12. Jung, D.-H.; Kwon, J.-K.; Woo, N.-S.; Kim, Y.-J.; Goto, M.; Kim, S. S–N fatigue and fatigue crack propagation behaviors of X80 steel at room and low temperatures. *Metall. Mater. Trans. A* **2014**, *45*, 654–662. [CrossRef]
13. Tong, L.; Niu, L.; Ren, Z.; Zhao, X.L. Experimental investigation on fatigue behavior of butt-welded high-strength steel plates. *Thin-Walled Struct.* **2021**, *165*, 107956. [CrossRef]
14. Hariprasath, P.; Sivaraj, P.; Balasubramanian, V.; Srinivas, P.; Sridhar, K. Influence of stress ratio on fatigue behaviour of gas metal arc welded naval grade HSLA steel joints: Assessment of safe and unsafe region for ship hull fabrication. *Eng. Fail. Anal.* **2023**, *148*, 107216. [CrossRef]
15. Moravec, J.; Sobotka, J.; Novakova, I.; Bukovska, S. Assessment the partial welding influences on fatigue life of S700MC steel fillet welds. *Metals* **2021**, *11*, 334. [CrossRef]
16. Ilic, A.; Ivanović, L.; Lazić, V.; Josifović, D. Welding method as influential factor of mechanical properties at high-strength low-alloyed steels. *IOP Conf. Ser. Mater. Sci. Eng.* **2019**, *659*, 012036. [CrossRef]
17. Hochhauser, F.; Ernst, W.; Rauch, R.; Vallant, R.; Enzinger, N. Influence of the soft zone on the strength of welded modern HSLA steels. *Weld. World* **2012**, *56*, 77–85. [CrossRef]
18. Nowacki, J.; Sajek, A.; Matkowski, P. The influence of welding heat input on the microstructure of joints of S1100QL steel in one-pass welding. *Arch. Civ. Mech. Eng.* **2016**, *16*, 777–783. [CrossRef]
19. Vimalraj, C.; Kah, P.; Layus, P.; Belinga, E.M.; Parshin, S. High-strength steel S960QC welded with rare earth nanoparticle coated filler wire. *Int. J. Adv. Manuf. Technol.* **2019**, *102*, 105–119. [CrossRef]
20. Denisa, M.; Michal, J.; Tibor, V.; Lýdia, F.D.; František, N. Examination of fatigue life of HSLA Domex 700 MC welded joints. *Transp. Res. Procedia* **2021**, *55*, 533–537. [CrossRef]
21. Stoschka, M.; Leitner, M.; Posch, G.; Eichlseder, W. Effect of high-strength filler metals on the fatigue behaviour of butt joints. *Weld. World* **2013**, *57*, 85–96. [CrossRef]

22. Maurya, A.K.; Chhibber, R.; Pandey, C. Heat input effect on dissimilar super duplex stainless steel (UNS S32750) and nitronic steel (n 50) gas tungsten arc weld: Mechanism, microstructure, and mechanical properties. *J. Mater. Eng. Perform.* **2023**, *32*, 5283–5316. [CrossRef]
23. Moshtaghi, M.; Loder, B.; Safyari, M.; Willidal, T.; Hojo, T.; Mori, G. Hydrogen trapping and desorption affected by ferrite grain boundary types in shielded metal and flux-cored arc weldments with Ni addition. *Int. J. Hydrogen Energy* **2022**, *47*, 20676–20683. [CrossRef]
24. *ASTM E3-01*; Standard Guide for Preparation of Metallographic Specimens. ASTM International: West Conshohocken, PA, USA, 2001.
25. *ASTM E8/E8M-22*; Standard Test Methods for Tension Testing of Metallic Materials. ASTM International: West Conshohocken, PA, USA, 2022.
26. *ASTM E466-21*; Standard Practice for Conducting Force Controlled Constant Amplitude Axial Fatigue Tests of Metallic Material. ASTM Standards: Philadelphia, PA, USA, 2021.
27. Haupt, W. Avaliação Geométrica e Microestrutural de Soldas em Aços de Alta Resistência Aplicados na Indústria Agrícola. In *Anais do Congresso Internacional de Engenharia Mecânica e Industrial*; Anais. São Paulo (SP) CREA-SP, 2022; Even3: Recife, Brazil, 2023. Available online: https//www.even3.com.br/anais/xxiiconemi/570032-AVALIACAO-GEOMETRICA-E-MICROESTRUTURAL-DE-SOLDAS-EM-ACOS-DE-ALTA-RESISTENCIA-APLICADOS-NA-INDUSTRIA-AGRICOLA (accessed on 6 July 2023).
28. Thewlis, G. Classification and quantification of microstructures in steels. *Mater. Sci. Technol.* **2004**, *20*, 143–160. [CrossRef]
29. Shi, S.-C.; Wang, W.-C.; Ko, D.-K. Influence of inclusions on mechanical properties in flash butt welding joint of high-strength low-alloy steel. *Metals* **2022**, *12*, 242. [CrossRef]
30. Lee, S.G.; Kim, B.; Sohn, S.S.; Kim, W.G.; Um, K.K.; Lee, S. Effects of local-brittle-zone (LBZ) microstructures on crack initiation and propagation in three Mo-added high-strength low-alloy (HSLA) steels. *Mater. Sci. Eng. A* **2019**, *760*, 125–133. [CrossRef]
31. Mirzaei, M.; Jeshvaghani, R.A.; Yazdipour, A.; Zangeneh-Madar, K. Zangeneh-Madar. Study of welding velocity and pulse frequency on microstructure and mechanical properties of pulsed gas metal arc welded high strength low alloy steel. *Mater. Des.* **2013**, *51*, 709–713. [CrossRef]
32. Ngoula, D.T.; Beier, H.T.; Vormwald, M. Fatigue crack growth in cruciform welded joints: Influence of residual stresses and of the weld toe geometry. *Int. J. Fatigue* **2017**, *101*, 253–262. [CrossRef]
33. Gordon, J.V.; Haden, C.V.; Nied, H.F.; Vinci, R.P.; Harlow, D.G. Fatigue crack growth anisotropy, texture and residual stress in austenitic steel made by wire and arc additive manufacturing. *Mater. Sci. Eng. A* **2018**, *724*, 431–438. [CrossRef]
34. Ribeiro, H.V.; Baptista, C.A.R.P.; Lima, M.S.F.; Torres, M.A.S.; Marcomini, J.B. Effect of laser welding heat input on fatigue crack growth and CTOD fracture toughness of HSLA steel joints. *J. Mater. Res. Technol.* **2021**, *11*, 801–810. [CrossRef]
35. Hariprasath, P.; Sivaraj, P.; Balasubramanian, V.; Pilli, S.; Sridhar, K. Effect of the welding technique on mechanical properties and metallurgical characteristics of the naval grade high strength low alloy steel joints produced by SMAW and GMAW. *CIRP J. Manuf. Sci. Technol.* **2022**, *37*, 584–595. [CrossRef]
36. Kim, Y.; Hwang, W. Effect of weld seam orientation and welding process on fatigue fracture behaviors of HSLA steel weld joints. *Int. J. Fatigue* **2020**, *137*, 105644. [CrossRef]

Disclaimer/Publisher's Note: The statements, opinions and data contained in all publications are solely those of the individual author(s) and contributor(s) and not of MDPI and/or the editor(s). MDPI and/or the editor(s) disclaim responsibility for any injury to people or property resulting from any ideas, methods, instructions or products referred to in the content.